Molecular design for tailoring single source precursor for bismuth ferrite

Georg Bendt,[a] Rafael Schiwon,[c] Soma Salamon,[b] Joachim Landers,[b] Ulrich Hagemann,[d] Christian Limberg,[c] Heiko Wende[b] and Stephan Schulz[a*]*

[a] Faculty of Chemistry, Inorganic Chemistry, and Center for Nanointegration Duisburg-Essen (CENIDE), University of Duisburg-Essen, Universitätsstr. 7, 45114 Essen, Germany; [b] Faculty of Physics and Center for Nanointegration Duisburg-Essen (CENIDE), University of Duisburg-Essen, Lotharstr. 1, 47048 Duisburg, Germany; [c] Institut für Chemie, Humboldt-Universität zu Berlin, Brook-Taylor-Str. 2, 12489 Berlin, Germany; [d] Interdisciplinary Center for Analytics on the Nanoscale (ICAN), NETZ, Carl-Benz-Str. 199, 47047 Duisburg, Germany.

KEYWORDS. Single source precursor, bismuth ferrite, magnetic properties

ABSTRACT. Nearly phase-pure bismuth ferrite particles were formed by the thermolysis of the *single source precursor* $[Cp(CO)_2Fe\text{-}Bi(OAc)_2]$ **1** in octadecene at 245 °C, followed by subsequent calcination at 600 °C for 3 h. In contrast, the slightly modified compound $[Cp(CO)_2Fe\text{-}Bi(O_2C^tBu)_2]$ **2** yielded only mixtures of different bismuth oxide phases, revealing the distinctive influence of molecular design in material synthesis. The chemical composition, morphology and crystallinity of the resulting materials were investigated by XRD, TEM and EDX. In addition, the optical properties were investigated by FTIR- and UV-Vis spectroscopy

showing a strong band gap absorption in the visible range at 590 nm (2.2 eV). The magnetic behavior was probed by VSM and SQUID magnetometry, as well as ^{57}Fe Mössbauer spectroscopy.

Introduction

The use of single source precursors (SSP) as starting compounds for the formation of nanoparticles and thin films are a promising alternative approach for the synthesis of high quality materials.[1,2,3] SSPs already contain the elements of the desired material in a single molecule and their thermal properties and decomposition pathways can be modified by the precursor design, in particular the loss of highly volatile elements during synthesis resulting in off-stoichiometric products can be avoided. $BiFeO_3$ combines antiferromagnetic and ferroelectric behavior and belongs to the family of so-called multiferroics.[4] To the best of the author's knowledge, $BiFeO_3$ is the only multiferroic material which retains its properties above room temperature with a Néel temperature T_N = 370 °C and a Curie temperature T_C = 830 °C. $BiFeO_3$ crystallizes in the rhombohedrally distorted perovskite structure with lattice constants a = 5.58 Å and c = 13.87 Å in the hexagonal representation. The multiferroic nature can be explained by the displacement of Fe^{3+} and Bi^{3+} along the c-axis and a canted ordering of the Fe^{3+} spins leading to a cycloidal spin ordering with a period length of 62 nm.[5,6,7] $BiFeO_3$ exhibits a bandgap (2.1 – 2.8 eV) in the visible range, making it an ideal candidate photocatalyst for the degradation of organic molecules[8,9,10] or water splitting, too.[11,12]

The synthesis of $BiFeO_3$ is afflicted with several problems; the ternary bismuth iron oxygen phase diagram shows multiple bismuth-rich phases including $Bi_2Fe_4O_9$ and $Bi_{25}FeO_{40}$, which are often seen parasitic phases. Furthermore, a high leak current due to defects, mostly oxygen vacancies and impurities (Fe^{2+} ions) limits the technical application.[13,14] Several synthetic

strategies have been developed for the formation of $BiFeO_3$, including solid-state reactions,[15] sol-gel,[16] hydrothermal as well as microwave assisted hydrothermal,[17] self-combustion[18] and electrospinning.[19] The most common precursors are bismuth and iron nitrates. However, while single source precursors for the solution based synthesis of $BiFeO_3$ are unknown, to date, Blackman et al. investigated the heterobimetallic compound $[Cp(CO)_2FeBiCl_2]$ (Cp = η^5-C_5H_5) as AACVD (aerosol-assisted chemical vapor deposition) precursor for the deposition of $BiFeO_3$ on different substrates at 300°C with subsequent annealing at 500 – 700 °C.[20] The phase-pure films obtained at 700 °C exhibit a direct bandgap at 2.1 eV and high activity for water oxidation under visible light irradiation.

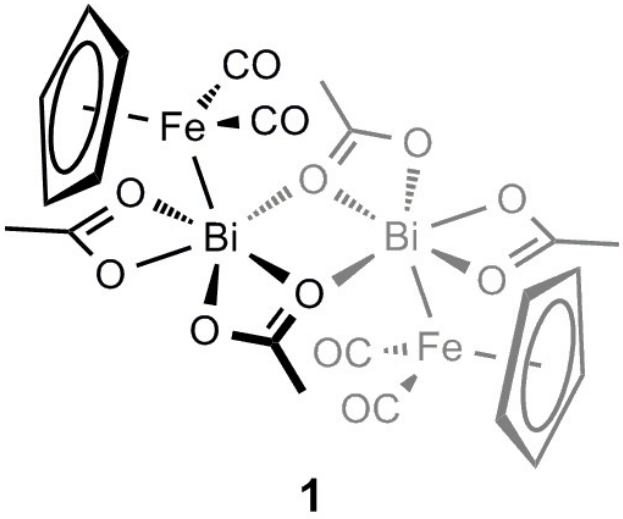

1

Figure 1. Fe-Bi Compound **1**.[22]

Recently, we reported a precedent case proving that molecular Fe–Bi entities can be constructed by reactions of complexes with Fe–Fe bonds and bismuth carboxylates: The reaction between $[Cp(CO)_2Fe]_2$ and $[Bi(OAc)_3]$ yielded $[Cp(CO)_2Fe–Bi(OAc)_2]$, **1** (Fig. 1).[21] Here we now describe our results testing **1** as well as the newly prepared derivative $[Cp(CO)_2Fe–Bi(O_2C^tBu)_2]$, **2**, varying in the carboxylate residue, as SSPs.

Results and discussion

After the successful preparation of **1** we have been able to show that setting out from $[Cp(CO)_2Fe]_2$ ($[Fp]_2$) also $[Fp{-}Bi(O_2CH)_2]_n$ is accessible via reaction with bismuth formate;[21b] due to aggregation to a coordination polymer the product was only sparingly soluble in common organic solvents, though. Aiming at soluble derivatives and further support, that indeed reactions of $[Fp]_2$ with bismuth carboxylates provide a more general access to molecular Bi/Fe compounds, we have thus treated $[Cp(CO)_2Fe]_2$ with bismuth pivalate instead of bismuth acetate. Stirring of an equimolar $[Fp]_2$ / $[Bi(O_2C^tBu)_3]$ suspension in dichloromethane at room temperature for a period of 9 days resulted in a red solution, which was evaporated to dryness to yield a brown powder. Washing the residue with small portions of hexane and crystallization from a dichloromethane / hexane mixture led to red crystals of $[Cp(CO)_2Fe\text{-}Bi(O_2C^tBu)_2]$ **2** in 53 % yield. A single-crystal X-ray diffraction analysis revealed that **2** crystallizes as a dimer (with a crystallographic inversion center) similar to that of the acetate **1** (Fig. 2).

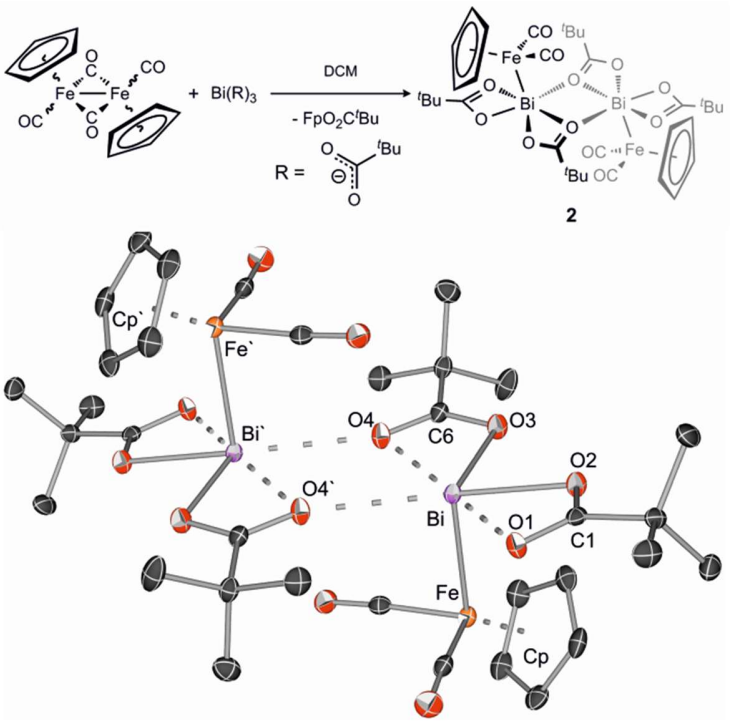

Figure 2. Synthesis of **2** by reaction of $[Fp]_2$ with $[Bi(O_2C^tBu)_3]$ and molecular structure of **2**. Displacement ellipsoids are shown at the 50 % probability level. Hydrogen atoms are omitted for clarity. Selected bond lengths (Å) and angles (°): Fe−Bi 2.6072(4), Bi−O2 2.2978(18), Bi−O3 2.3277(18), Bi···O1 2.6298(17), Bi···O4 2.6312(17), Bi···O4' 2.7971(18), C1−O1 1.249(3), C1−O2 1.285(3), C6−O4 1.251(3), C6−O3 1.286(3), Bi···Bi' 4.4989(4); Cp−Fe−Bi 122.919(16), O2−Bi−O3 79.73(6), O2−Bi−Fe 95.09(5), O3−Bi−Fe 95.23(5), O2−Bi···O4' 157.455(60), O1···Bi···O4 171.07(6).

Each bismuth atom is bound to one organometallic iron fragment via a Fe-Bi metal bond (2.6072(4) Å), which is longer than the corresponding distance in **1** (Fe−Bi: 2.585(2) Å). Additionally two covalent bonds to two pivalate ligands are formed (Bi−O2: 2.2978(18), Bi−O3: 2.3277(18) Å) with distances that are also longer than the corresponding distances in **1** (d(Bi-O) = 2.342-2.353 Å). The angle between these O atoms (O2–Bi–O3: 79.73(6) Å) and also all Fe–Bi–O angles (92.56(4)–95.23(5)◦) indicate that these covalent bonds are mainly established through p orbitals at the Bi atom. The corresponding carbonyl units of the carboxylate ligands also interact with the respective Bi centers, and one of them per molecule is further involved in a secondary Bi···O-Bi'-contact with the Bi atom of a second molecule (O4'···Bi, O4···Bi' 2.7971(18) Å). As the second molecule bonds back via an analogous interaction, a dimer is thus created featuring a $[Bi_2O_2]$ diamond core motif with larger Bi-O' and Bi···Bi' distances (4.4989(4) Å) compared to those in **1** (d(Bi-O') = 2.711(4) Å, d(Bi-Bi') = 4.3485(6) Å).

Fig. 3 displays the results obtained from thermogravimetric investigations (see also Figs. S1, S2 in Supplementary Material) showing that the compounds **1** and **2** cannot be transferred into the gas phase under normal pressure without decomposition, so that determination of its potential as

an SSP for CVD requires more studies under authentic conditions. We have therefore examined its behavior as an SSP in solution, as described below.

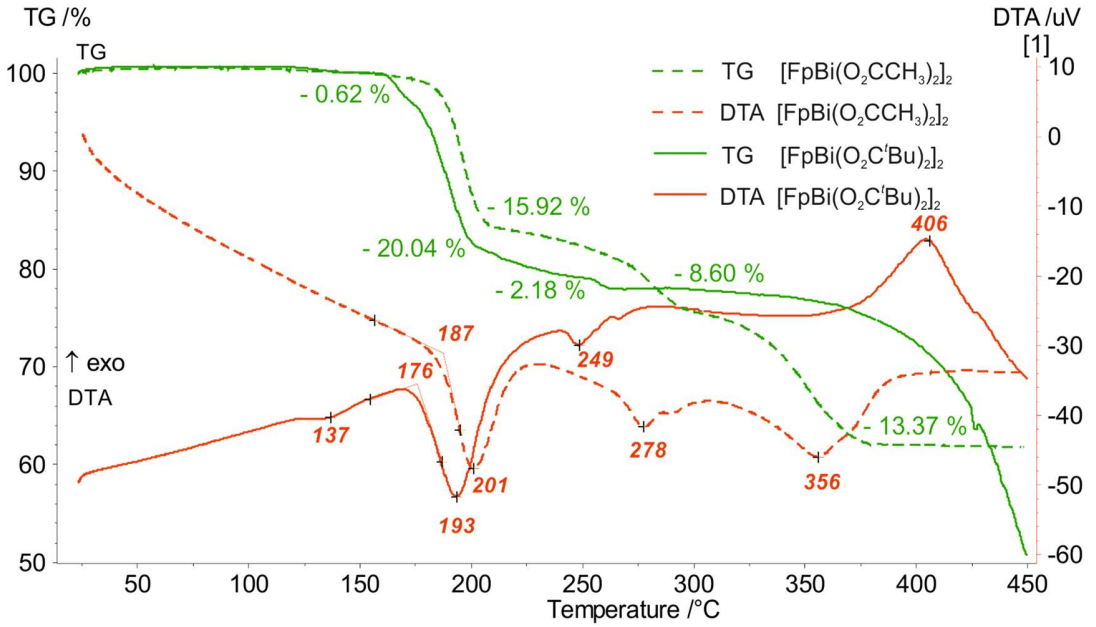

Figure 3. STA measurement (argon purge gas, 60 mL / min, heating rate 10 K / min) of $FpBi(O_2CCH_3)_2$ **1** (dashed lines) and $FpBi(O_2C^tBu)_2$ **2** (solid lines). Thermogravimetric analysis (TA) is shown in green, differential thermal analysis (DTA) is shown in red.

Thermolysis reactions were performed first with 200 mg of **1** which was suspended in 10 mL octadecene, slowly heated to 215, 230 and 245 °C, respectively, in order to investigate the role of the reaction temperature and stirred for 1 h. The orange suspension turned to a black suspension around 200 °C. After cooling to ambient temperature, the decomposition products were isolated by centrifugation and repeatedly washed with chloroform. The chemical composition of the resulting materials was analyzed by EDX. The product obtained at 245 °C shows a composition of 20 at% Bi, 20 at% Fe and 60 at% O, corresponding to a Bi:Fe atomic ratio close to 1, indicating the complete decomposition of the precursor, while the products obtained at lower

temperatures are Bi-rich. In addition, the EDX analyses of all three samples reveal high carbon contents, which are not taken into account, indicating the presence of organic groups.

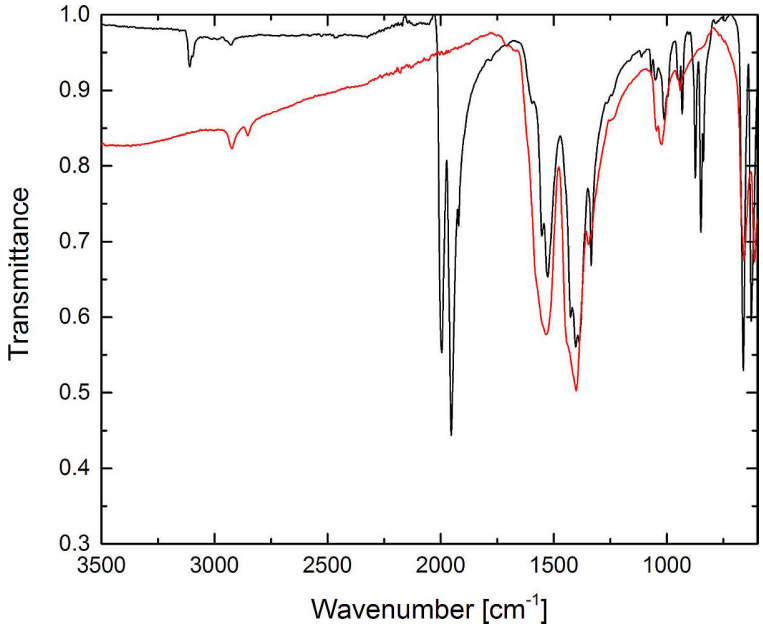

Figure 4. FTIR spectra of precursor **1** (black) and the decomposition product obtained at 245 °C after workup (red).

The samples were further investigated by IR spectroscopy. In Fig. 4, the IR spectra of precursor **1** (black) and the decomposition product as-obtained at 245 °CD (red) are displayed. Compared to the precursor, the black powder shows the loss of the characteristic absorption bands around 2000 cm^{-1} for the carbonyl ligands, whereas the bands for the carboxylate group around 1500 cm^{-1} are still present.

In order to obtain crystalline $BiFeO_3$, the amorphous black powders were annealed at 600 °C for 3 h in air. The resulting products showed the characteristic orange color of $BiFeO_3$.

The XRD patterns of the annealed powders are displayed in Fig. 5. The powders obtained at 215 and 230 °C after annealing consist of different phases with $BiFeO_3$ (PDF 71-2494) as major phase and $Bi_2Fe_4O_9$ (PDF 71-2494) and $Bi_{25}FeO_{40}$ (PDF 71-2494) as minor phases. The results

of the quantitative phase analysis are displayed in Table 1. In contrast, the pattern of the annealed powder obtained at 245 °C can be indexed on the basis of rhombohedrally distorted perovskite structure, which indicates the formation of nearly phase-pure $BiFeO_3$. The origin of the formation of Bi-rich phases can be found in the high Bi content of the decomposition product. The bismuth content is lower than in the as-decomposed products indicating the loss of Bi or Bi_2O_3 due their high vapor pressure.

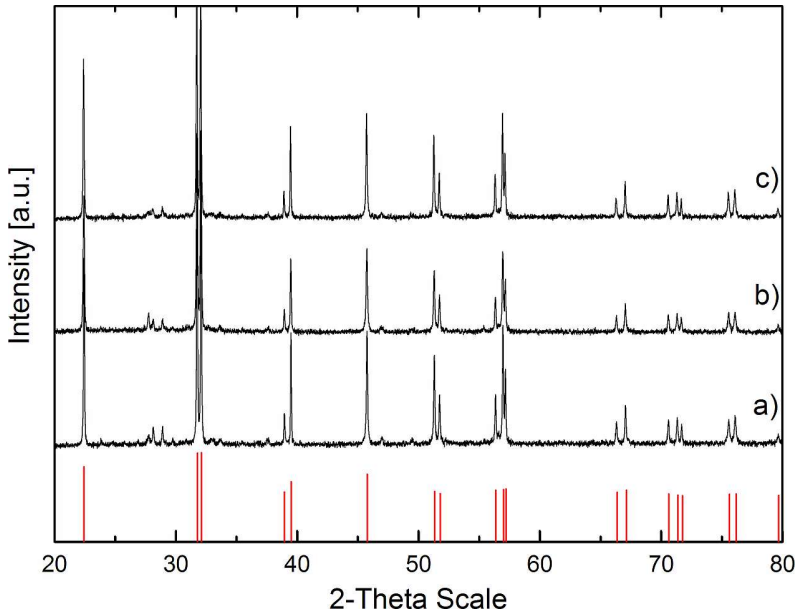

Figure 5. Powder X-ray diffractograms of $BiFeO_3$ particles obtained by calcination of the decomposition product from precursor **1** at different temperatures (a 215 °C, b 230 °C, c 245 °C, red: $BiFeO_3$, PDF 71-2494) in octadecene.

Table 1. Bi : Fe ratios for different samples as determined by EDX measurements and the results of the quantitative Rietveld refinement for the samples.

Sample No.	Precursor	T_{decomp}	Bi:Fe ratio[a]	Bi:Fe ratio[b]	Phases[c]
I	1	215	62:38	58:42	93.5 wt% $BiFeO_3$ 6.5 wt% $Bi_2Fe_4O_9$

II	1	230	57:43	54:46	87.7 wt% $BiFeO_3$ 8.6 wt% $Bi_2Fe_4O_9$ 3.4 wt% $Bi_{25}FeO_{39}$
III	1	245	53:47	51:49	82.0 wt% $BiFeO_3$ 12.6 wt% $Bi_2Fe_4O_9$ 5.4 wt% $Bi_{25}FeO_{39}$
IV	2	215	100:0	100:0	Bi_2O_3
V	2	245	100:0	100:0	Bi_2O_3

[a] EDX before calcination; [b] EDX after calcination; [c] as-determined by XRD.

The FTIR spectrum of the phase-pure $BiFeO_3$ (Fig. 6a) shows strong absorption bands around 530 and 430 cm^{-1} related to the characteristic stretching and bending of the Fe-O bonds in the FeO_6 octahedron, the main building block of the perovskite structure. In order to determine the band gap of the $BiFeO_3$ powder, UV-Vis diffuse reflectance spectra were recorded. Applying the Kubelka-Munk function leads to a band gap energy of 2.2 eV (Fig. 6b).

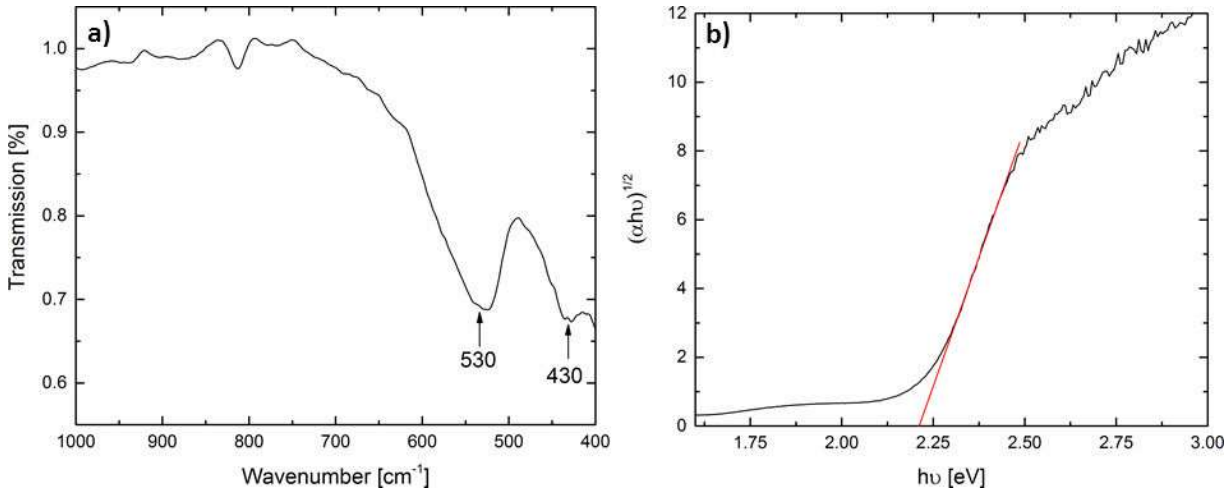

Figure 6. Typical IR spectrum of $BiFeO_3$ powder (a) and Tauc plot for determining the optical band gap (b).

Fig. 7 displays a typical TEM image obtained from the phase pure $BiFeO_3$ crystallites showing a relatively broad size distribution between 100 - 200 nm. The crystalline particles, which are electron transparent as can be seen in Fig. 7c, are sintered together due the thermal treatment

(annealing). HRTEM as well as selected area electron diffraction pattern (SAED) of a single particle demonstrate their high crystalline nature, as was expected from the PXRD studies.

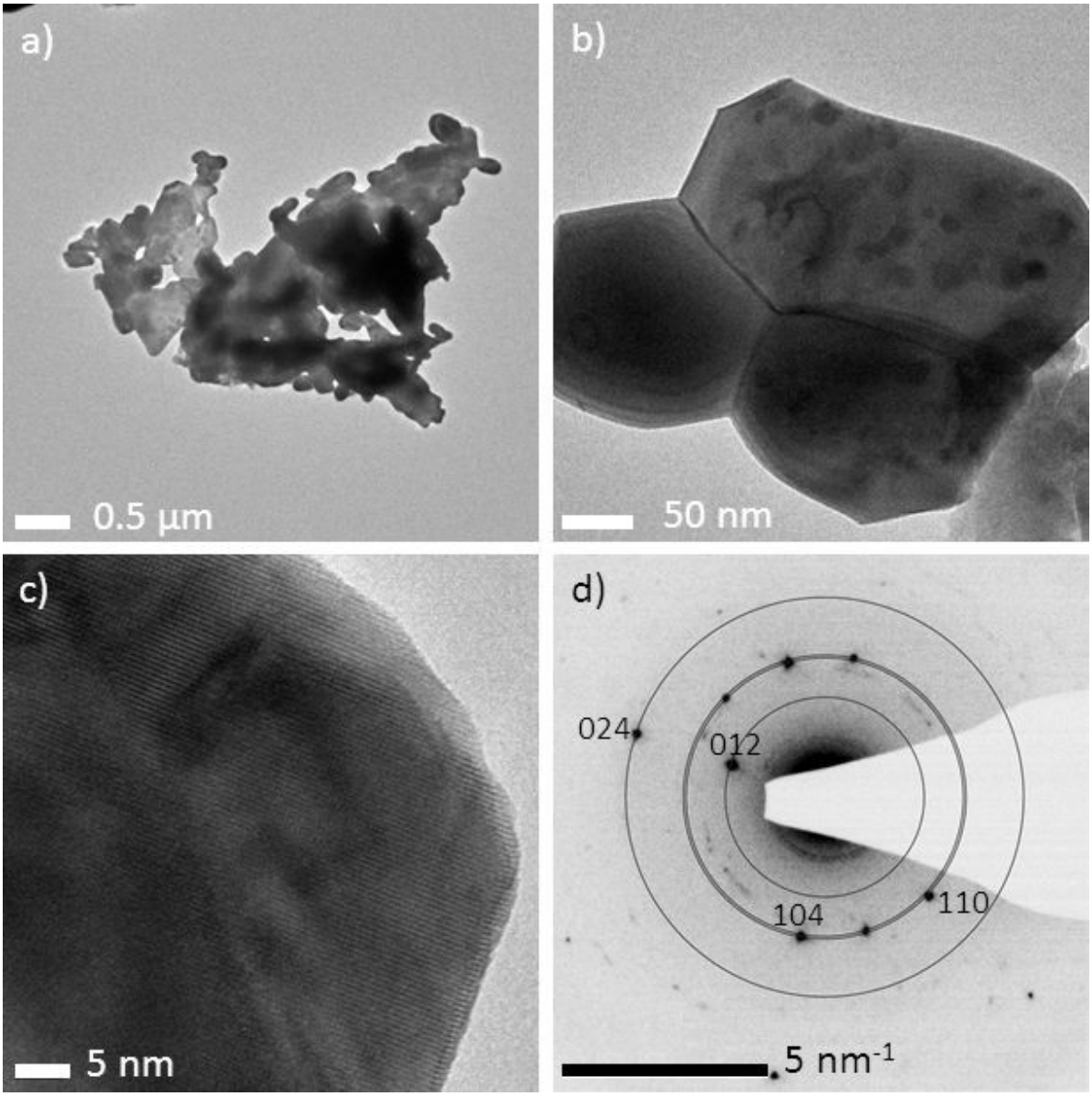

Figure 7. TEM images (a-c) and the selected area electron diffraction pattern (SAED) of sample **III** (d); Scale bars 0.5 µm (a), 50 nm (b), 5 nm (c), 5 nm (d).

X-ray photoelectron spectroscopy (XPS) is very sensitive to the oxidation state of metals. The XPS measurement confirms the presence of bismuth, iron and oxygen. In addition, a small

amount of carbon is detected, which is not only adventitious carbon due to surface contamination as was shown by etching experiments but also originates from the material, indicating an incomplete decomposition precursor. The high resolution spectrum of the Bi4f peaks shows the characteristic peaks at 164 and 159 eV corresponding to Bi^{3+}. For iron, the Fe2p peaks at 724 and 710 eV, and especially the existence and position of the Fe2p satellite at 719 eV, indicate only the presence of Fe^{3+} cations; no peaks corresponding to Fe^{2+} are found (Fig. 8).

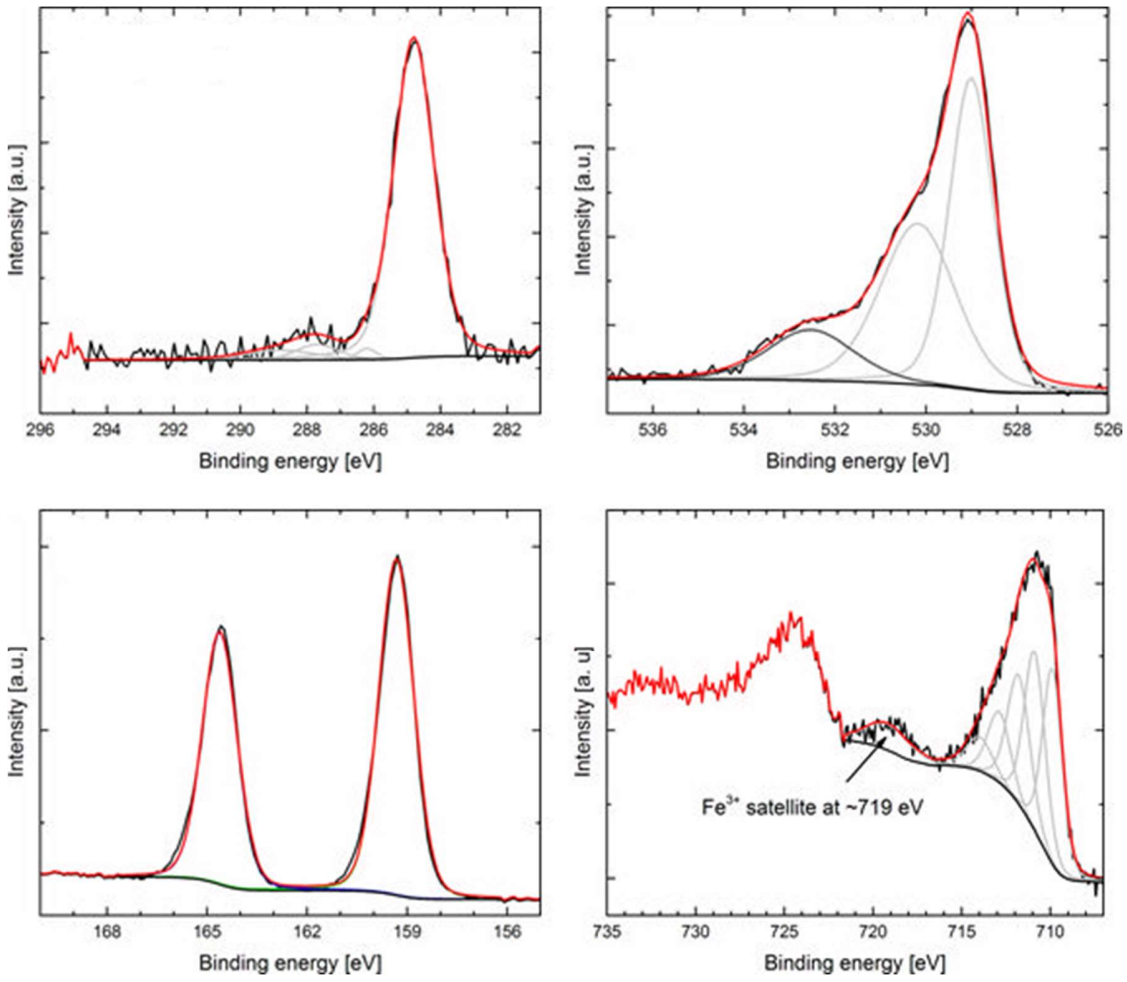

Figure 8. C 1s, O1s, Fe 2p and Bi 4f X-ray photoelectron spectra of $BiFeO_3$. Experimental Data (black), Envelope (red) and deconvoluted peaks (grey).

In order to investigate the influence of the precursor design on the decomposition pathway, **2** was also investigated as potential precursor for $BiFeO_3$ and the results were compared to those obtained with precursor **1**, which contains acetate instead of pivalate groups. The thermolysis reaction was performed with 200 mg of **2** suspended in 10 mL octadecene, slowly heated to 215 °C and 245 °C, respectively, and stirred for 1 h. The red suspension turned black around 200 °C. After cooling to ambient temperature, the decomposition products were isolated by centrifugation and repeatedly washed with chloroform.

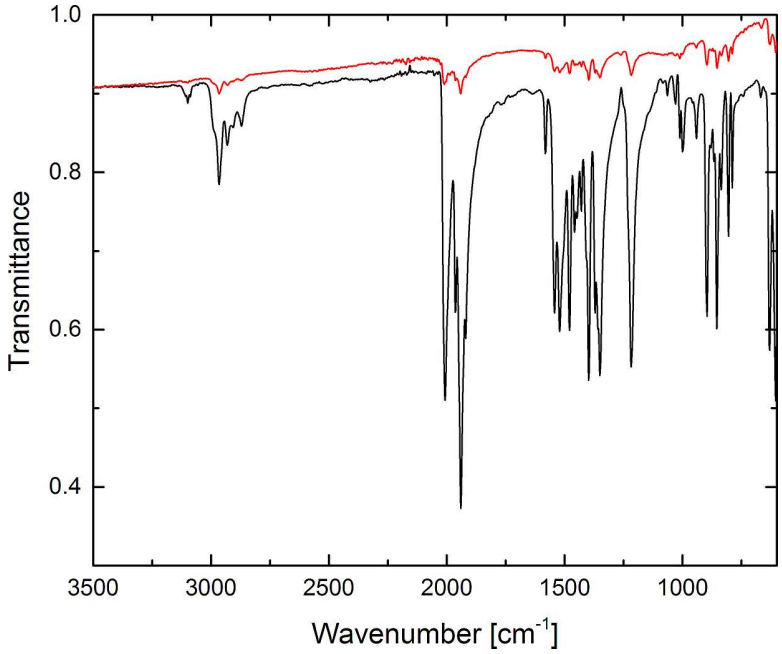

Figure 9. FTIR spectra of precursor **2** (black) and the decomposition product obtained at 245 °C after workup (red).

The chemical composition of resulting materials was analyzed by EDX (table 1). Both products, obtained at 215 as well as 245 °C showed only the presence of bismuth and carbon. The IR-spectra of the washed powder shows weak absorption bands indicating the presence of traces of intact precursor molecules (Fig. 9). After thermal treatment at 600 °C for 3 h, yellow powders were obtained. As expected from the EDX results of the black powder, the XRD pattern

showed the presence of Bi_2O_3 (PDF 41-1449) as major product and traces of the non-stoichiometric phase $Bi_2O_{2.33}$ (PDF 27-0051) (Fig. 10).

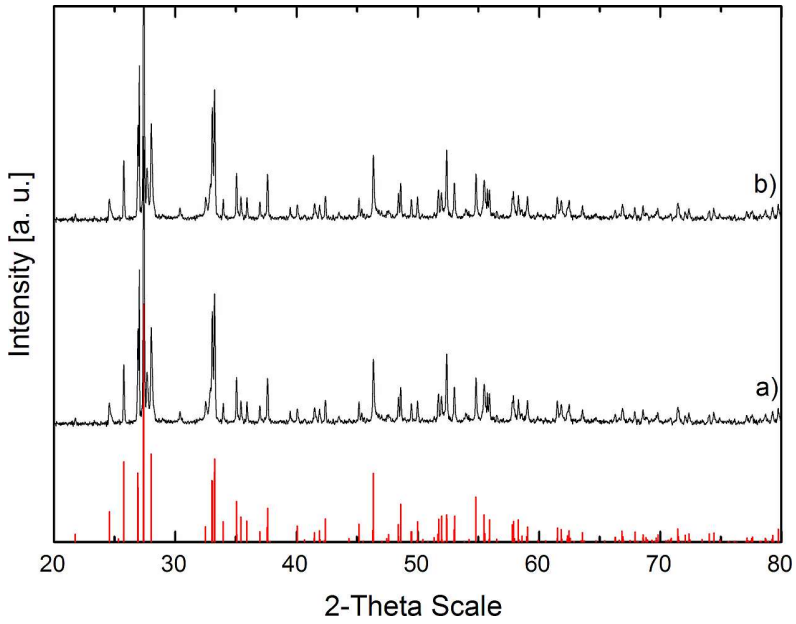

Figure 10. Powder X-ray diffractograms of Bi_2O_3 particles after calcination of the decomposition product from precursor **1** at different temperatures (a 215 °C, b 230 °C, c 245 °C, red: Bi_2O_3, PDF 41-1449).

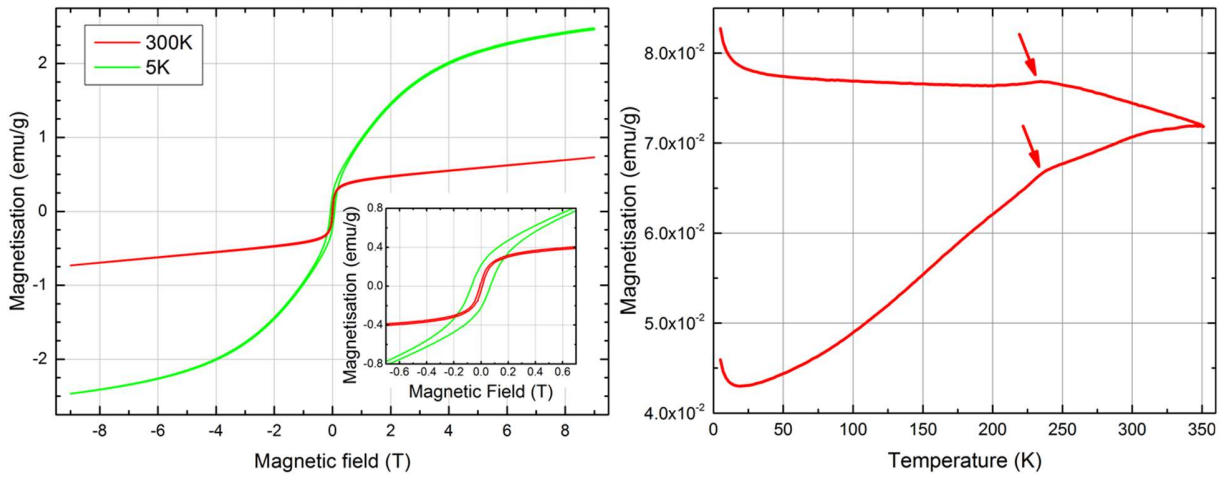

Figure 11. M(H) loops of sample **III** at 300 K and 5 K (left), the inset showing a magnification of the low-field regime, and a ZFC-FC M(T) measurement performed at 10mT (right).

Magnetic properties of sample **III** were investigated by VSM and SQUID magnetometry. The 300 K M(H) magnetisation curve displayed in Fig. 11 shows a linear response in the high field range, often seen in antiferromagnetic samples. In the low field range, a weak ferromagnetic signal due to canted antiferromagnetically coupled spins is visible. The maximum magnetisation at room temperature was determined to be 0.73 emu/g at 9 T, which is large compared to bulk-$BiFeO_3$, presumably due to uncompensated surface spins and size effects.[23] The 5 K magnetisation curve shows an open hysteresis that wasn't visible in the 300 K curve, indicating superparamagnetic behavior also visible in the temperature dependent magnetisation: The M(T) data shown in Fig. 11 reveals a clear splitting between field-cooled and zero-field-cooled magnetisation at low temperatures, corresponding to Néel relaxation behaviour of the smaller particles within the sample, in agreement with the beginning superparamagnetic doublet visible in the room temperature Mössbauer spectrum. Furthermore, a clear cusp is visible in both the ZFC and the FC curve at a temperature of 236K ± 3K, marked by arrows. This indicates the presence of a minor $Bi_2Fe_4O_9$ phase, as this material is reported to show an antiferromagnetic to paramagnetic transition in the range of about 250-260K,[24,25] presumably decreased here by size effects. Due to its antiferromagnetic behaviour, it has no noticeable influence on the M(H) curves shown earlier. The presence of a small amount of $Bi_2Fe_4O_9$ is also verified by Mössbauer spectroscopy, as described in detail below.

Table 2: Hyperfine parameters of sample **III** at 80 K: Hyperfine magnetic field B_{hf}, isomer shift δ relative to α-Fe at room temperature, nuclear quadrupole level shift 2ε, respectively quadrupole splitting ΔE_Q and relative spectral area A.

	B_{hf} (T)	**δ (mm/s)**	**$2\varepsilon/\Delta E_Q$ (mm/s)**	**A (%)**
$BiFeO_3$	54.07 ± 0.03	0.50 ± 0.01	0.14 ± 0.01	86.0 ± 0.6
$BiFeO_3$ sp.	---	0.18 ± 0.01	0.45 ± 0.01	5.2 ± 0.1
$Bi_2Fe_4O_9$ I	44.15 ± 0.05	0.32 ± 0.01	0.12 ± 0.01	4.7 ± 0.1
$Bi_2Fe_4O_9$ II	47.65 ± 0.05	0.44 ± 0.01	0.31 ± 0.02	4.7 ± 0.2

Mössbauer spectra were recorded at room temperature (300K), 80K and 4.3K, hyperfine parameters of the spectrum at 80 K are shown representatively in Table 2, displaying good agreement with data previously reported for $BiFeO_3$ (full details given in Table S1).[23,26,27] As visible in Fig. 12a, the room temperature spectrum is composed of a sextet corresponding to an antiferromagnetically coupled $BiFeO_3$ phase, and several (super-)paramagnetic doublets. The sextet displays a clearly visible asymmetry between opposite lines such as 1 and 6, which are often explained by an anisotropic hyperfine magnetic field, caused by the complex spin structure.[28] Latter leads to a distribution of hyperfine magnetic fields, which prevents successful fitting of the spectrum using a single sextet. Therefore, a distribution of hyperfine magnetic fields with 40 equidistant subspectra was used to achieve a precise congruence between measurement data and fit function. Due to the high Néel temperature of $BiFeO_3$, it is reasonable to assume that the dominant doublet is mainly caused by superparamagnetic behavior of the smallest $BiFeO_3$ particles contained in the sample.[26,29] This is supported by spectra at 4.3 (Fig. 12c) and 80 K (Fig. 12b), which reveal a decrease in the doublet spectral area from ca. 13 % at room temperature down to 5 % at 80 K. However, the isomer shift shows a strong decrease from

300 K to 80 K and little change from 80 K to 4.3 K (see Table S1). We therefore assume that the small residual contribution at low temperatures is caused by a minute paramagnetic Fe-bearing phase. The change in isomer shift means that the majority of the doublet at 300 K is caused by superparamagnetic $BiFeO_3$, which becomes magnetically blocked at 80 K. When closely examining the low velocity range at the centre of the room temperature spectrum, one can identify two additional doublets not belonging to the main $BiFeO_3$ doublet, matching hyperfine parameters of $Bi_2Fe_4O_9$ at room temperature.[30] This is further supported by the observation of two minor sextets of equal spectral area and with lower hyperfine magnetic fields compared to $BiFeO_3$ at 80 K and 4.3 K, with hyperfine parameters listed in Table 2, matching those of $Bi_2Fe_4O_9$.[31,32,33] Since $Bi_2Fe_4O_9$ has a higher Fe content than $BiFeO_3$, the combined relative spectral area (proportional to the number of Fe atoms) of ca. 9 % corresponds to only 5-6 wt%.

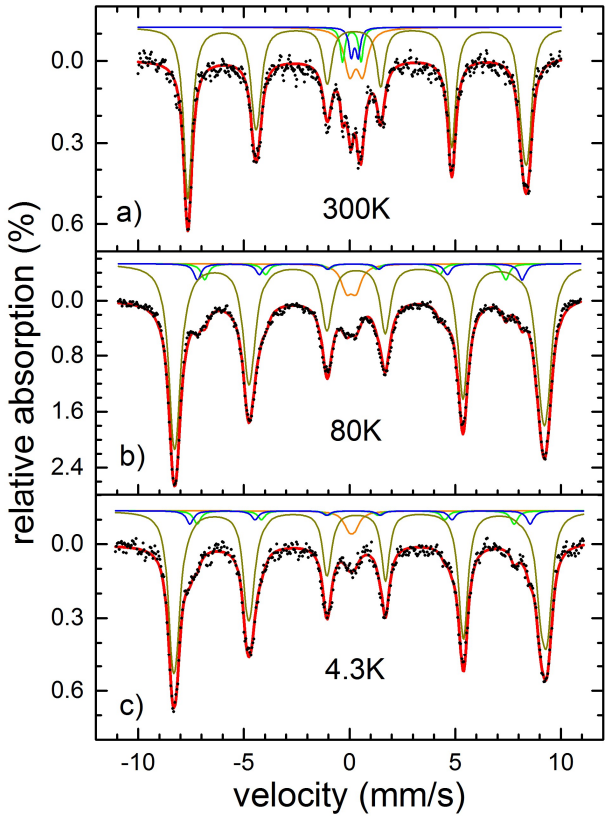

Figure 12. Mössbauer spectra recorded at 300 K (a), 80 K (b) and 4.3 K (c). Black symbols show experimental data, site I (tetrahedral) and II (octahedral) of $Bi_2Fe_4O_9$ (green, blue), magnetically coupled $BiFeO_3$ (brown) and superparamagnetic $BiFeO_3$ (orange), with the red line showing the overall theoretical spectrum.

Conclusions. First we report further precedence demonstrating that heterobimetallic Fe-Bi compounds can be obtained readily through reactions between $[Fp]_2$ and bismuthcarboxylates. We have then provided evidence that such complexes can indeed serve as SSP for the preparation of $BiFeO_3$ in the course of procedures involving thermal treatment. Notably, our results also show, that subtle changes within the precursor molecules have pronounced effects on the $BiFeO_3$ materials that are obtained, that is, the properties of the material generated is sensitively determined by the SSP, which motivates further efforts with respect to the modification of such systems.

Magnetometry indicates partial superparamagnetic behaviour and the presence of a minor $Bi_2Fe_4O_9$ phase, while the saturation magnetisation is slightly higher than that of bulk-$BiFeO_3$, presumably due to size/surface effects. These findings support results from Mössbauer spectroscopy and allow us to quantify the amount of $Bi_2Fe_4O_9$ to 5-6 wt%, while the $BiFeO_3$ parameters are in agreement with literature values. The determined amount of $Bi_2Fe_4O_9$ is in good agreement with the result of the quantitative Rietveld refinement.

Experimental

Synthetic procedures, materials and methods. Octadecene (Sigma-Aldrich) was carefully dried over Na/K alloy and was degassed prior to use. $[Cp(CO)_2Fe\text{-}Bi(OAc)_2]$ **1**[2] and $[Bi(O_2C^tBu)_3]$[3] were synthesized according to literature methods, while $[Fp]_2$ (99 % Acros

Organics) was used as received. All synthetic steps were performed under Ar atmosphere using standard Schlenk techniques.

η^5–Cyclopentadienyldicarbonyliron–bismuth–di–η^2–pivalate, 2. Solid $[Bi(O_2C^tBu)_3]$ (289.60 mg, 0.566 mmol, 1 equiv.) was added to a suspension of $[Fp]_2$ (200 mg, 0.566 mmol, 1 equiv.) in dichloromethane (10 mL) to give a red solution within 9 days at ambient temperature. Removing all volatiles at reduced pressure and washing the brown residue with tree portions of 2 mL hexane led to an orange powder, which was extracted with 9 mL dichloromethane in small portions. Concentration of the combined extracts to 3 mL and layering of the solution with 9 mL hexane resulted in the formation of red crystals of **2** within 7 days storing at -30 °C (yield: 177 mg, 0.301 mmol, 53 %). – ^{1}H NMR (C_6D_6, 300.13 MHz, 25 °C): δ = 4.15 (s, 5 H, C_5H_5), 1.33 (s, 18 H, $C(CH_3)_3$. $^{13}C\{^1H\}$ NMR (C_6D_6, 75.47 MHz): δ = 196.9 (2 C, *C*O), 187.5 (2 C, O(O)*C*C(CH$_3$)$_3$), 83.6 (5 C, C_5H_5), 41.1 (2 C, O(O)C*C*(CH$_3$)$_3$), 28.0 (2 C, *C*H$_3$). – IR (KBr): ν [cm^{-1}] = 3926 s, 3107 s, 3098 s, 3089 s, 2965 m, 2931 s, 2906 s, 2870 s, 2015 sst, 1987 m, 1964 st, 1942 sst, 1920 m, 1582 s, 1547 m, 1525 m, 1507 s, 1480 m, 1460 s, 1448 s, 1430 s, 1398 m, 1370 m, 1350 m, 1351 m, 1219 m, 1088 s, 1066 s, 1030 s, 1013 s, 1001 s, 940 s, 901 s, 896 m, 876 s, 855 m, 839 s, 835 s, 804 m, 789 s, 634 m, 606 m, 579 m, 572 m, 537 s. 505 s, 454 s. – Anal. (%) for $C_{17}H_{23}BiFeO_6$ (588.19): calcd. C 34.71, H 3.94; found C 35.02, H 3.90.

Single crystal X-ray diffraction. The data collection for **2** was performed with a BRUKER D8 VENTURE area detector using Mo-Kα radiation (λ = 0.71073 Å) and its crystallographic data is summerized in in Table S1. Multi-scan absorption corrections implemented in SADABS[34] were applied to the data. The structures were solved by intrinsic phasing (SHELXS-97)[35] and refined by full-matrix least square procedures on F2 with all measured reflections

(SHELXL-2014)[36] with anisotropic temperature factors for all non-hydrogen atoms. All hydrogen atoms were added geometrically and refined by using a riding model.

Thermolysis of 1 and 2. 200 mg (0.3 mmol) of the precursor was suspended in 10 mL DIPB and the suspension was heated to 215 °C (**1**, **2**), 230 °C (**1**, **2**) and 245 °C (**1**), respectively, for 1 h. After cooling to ambient temperature, the black precipitate was isolated by centrifugation and purified by repeated washing with *n*-hexane (2 - 3 times). The dried solid was loaded in a ceramic boat and heated in a tube furnace to 600 °C with a heating rate of 10 K/min for 3 h.

Characterization

Thermal analysis. A NETZSCH thermoanalyzer STA 409 C *Skimmer®* system, equipped with a BALZERS QMG 421, was used to record the thermoanalytical curves. Further experimental details were as follows: DTA-TG sample carrier system; Pt/PtRh10 thermocouples; platinum crucibles (beaker, 0.8 ml); sample mass 20-30 mg (measured versus empty reference crucible); constant purge gas flow of 100 ml/min argon 5.0 (AIRLIQUIDE); constant heating rate 10 K/min; raw data evaluation with manufacturer's software PROTEUS® (v. 4.3) without further data treatment, e.g. such as smoothing.

X-ray Powder Diffraction (XRD). XRD patterns were obtained at ambient temperature (25 ± 2 °C) using a Bruker D8 Advance powder diffractometer in Bragg−Brentano mode with Cu K_α radiation (λ = 1.5418 Å, 40 kV, and 40 mA). The powder samples were investigated in the range of 5 to 90° 2θ with a step size of 0.01° 2θ and a counting time of 0.3 s. Rietveld refinement was performed with the program package TOPAS 4.2 from Bruker.

EDX Analysis. EDX studies were performed with a Jeol JSM 6510 scanning electron microscope equipped with an energy-dispersive X-ray spectroscopy (EDX) device (Bruker Quantax 400).

TEM Analysis. Transmission electron microscopy (TEM) measurements and selected area electron diffraction (SAED) were carried out on a Philips CM200 LaB_6 microscope operated at 200 kV. Samples for TEM observations were prepared by depositing a drop of a suspension of the material in ethanol onto a carbon-coated copper grid.

Magnetometry. Temperature dependent magnetic measurements between 5 and 350 K were performed using a Quantum Design MPMS-5S, while the field dependent M(H) loops up to 9 T were recorded by a Quantum Design PPMS DynaCool using powder samples.

Mössbauer Spectroscopy. Mössbauer spectra were recorded in transmission geometry using a constant-acceleration spectrometer with a ^{57}Co source embedded in a Rh matrix. $BiFeO_3$ powder was mixed with chemically inert boron nitride to obtain a sample with ca. 20mg/cm^2 $BiFeO_3$. Measurements below room temperature were performed in a liquid helium bath cryostat, while all spectrometers were calibrated using α-Fe foil at room temperature. The experimental spectra were least-squares fitted using the software package "Pi" by Ulrich von Hörsten.[37]

ASSOCIATED CONTENT

Supporting Information. CCDC 1446539 (**2**) contains the supplementary crystallographic data for this paper. These data can be obtained free of charge from The Cambridge Crystallographic Data Centre via www.ccdc.cam.ac.uk/data_request/cif.

AUTHOR INFORMATION

Corresponding Author

* To whom correspondence should be addressed. E-Mail: stephan.schulz@uni-due.de; christian.limberg@chemie.hu-berlin.de

Author Contributions

The manuscript was written through contributions of all authors. All authors have given approval to the final version of the manuscript.

Funding Sources

This work was supported by the DFG (SPP1681, WE2623/7-1, WE2623/13-2) and by Stiftung Mercator (MERCUR).

ACKNOWLEDGMENT

Financial support by the University of Duisburg-Essen is acknowledged by S. Schulz and H. Wende, while C. Limberg is grateful to the Humboldt-Universität zu Berlin for core support. We thank Prof. Barcikowski, University of Duisburg-Essen, for the UV-VIS spectrum, Prof. Pinna, Humboldt-Universität zu Berlin, for recording the TEM image, and Nicolas Frank, Humboldt-Universität zu Berlin, for the single crystal X-ray diffraction study, and Dr. Michael Feist for the TGA.

REFERENCES

[1] a) Martin, L. W.; Chu, Y.-H.; Ramesh, R. *Mater. Sci. Eng. R* **2010**, *68*, 89–133; b) Singh, M. K.; Yang, Y.; Takoudis, C. G. *Coord. Chem. Rev*. **2009**, *253*, 2920-2934; c) Zhang, Q.; Sando, D.; Nagarajan, V. *J. Mater. Chem. C* **2016**, *4*, 4092-4124.

[2] a) Bendt, G.; Weber, A.; Heimann, S.; Assenmacher, W.; Prymak O.; Schulz, S. *Dalton Trans.* **2015**, *44*, 14272-14280; b) Bendt, G.; Schulz, S.; Zastrow, S.; Nielsch, K. *Chem. Vap. Deposition* **2013**, *19*, 235–241; c) Schulz, S.; Heimann, S.; Friedrich, J.; Engenhorst, M.; Schierning, G., Assenmacher, W. *Chem. Mater.* **2012**, *24*, 2228-2234.

[3] a) Lieberman, C. M.; Wei, Z.; Filatov, A. S.; Dikarev, E. V. *Inorg. Chem*. **2016**, *55*, 3946–3951; b) Moniz, S. J. A.; Pugh, D.; Blackman, C. S.; Tang, J.; Carmalt, C. *J. Cryst. Growth Des*. 2016, doi: 10.1021/acs.cgd.6b00370.

[4] Catalan, G.; Scott, J. F. *Adv. Mater.* **2009**, *21*, 2463−2485.

[5] Fischer, P.; Polomska, M.; Sosnowska, I.; Szymanski, M. *J. Phys. C: Solid St. Phys.* **1980**, *18*, 1931-1940.

[6] Sosnowska, I.; Peterlin-Neumaier, T.; Streichele, E. *J. Phys. C: Solid St. Phys.* **1982**, *15*, 4835-4846.

[7] Landers, J.; Salamon, S.; Escobar Castillo, M.; Lupascu, D. C.; Wende, H. *Nano Lett.* **2014**, *14*, 6061−6065.

[8] Shaibani, P.M.; Prashanthi, K.; Sohrabi, A.; Thundat, T. *J. Nanotechnology* **2013**, 1-6.

[9] Wang, L.; Han, Y.; Jia, G.; Zhang, C.; Liu, Y.; Liu, L.; Wang, C.; Cao, X.; Yin, K. *J. Nanosci. Nanotechnol*. **2011**, *11*, 5207-5209.

[10] Gao, F.; Chen, X.; Yin, K.; Dong, S.; Ren, Z.; Yuan, F.; Yu, T.; Zou. Z.; Lin, J.-M. *Adv. Mater*. **2007**, *19*, 2889-2892.

[11] Moniz, S. J.; Blackman, C. S.; Southern, P.; Weaver, P. M.; Tang, J.; Carmalt, C. J. *Nanoscale* **2015**, *7*, 16343-16353.

[12] Li, S.; Zhang, J.; Kibria, M. G.; Mi, Z.; Chaker, M.; Ma, D.; Nechache, R.; Rosei, F. *Chem. Commun*. **2013**, *49*, 5856-5858.

[13] Ederer, C.; Spaldin, N. A. *Phys. Rev. B* **2005**, *71*, 224103.

[14] Dho, J.; Qi, X.; Kim, H.; MacManus-Driscoll, J. L.; Blamire, M. G. *Adv. Mater.* **2006**, *18*, 1445-1448.

[15] Bernado, M. S.; Jardiel, T.; Peiteado, M.; Caballero, A. C.; Villegas, M. *J. Eur. Ceram. Soc*. **2011**, *31*, 3047-3053.

[16] Xu, J.-H.; Ke, H.; Jia, D.-C.; Wang, W.; Zhou, Y. *J. Alloys. Compd*. **2009**, *472*, 473-477.

[17] Prando-Gonjal, J.; Villafuerte-Castrejon, M. E.; Fuentes, L.; Moran, E. *Mater. Res. Bull*. **2009**, *44*, 1734-1737.

[18] a) Wu, J.; Mao, S.; Ye, Z.-G.; Xie, Z.; Zheng, L. *J. Mater. Chem*. **2010**, *20*, 6512-6516; b) Ortiz-Quiñonez, J. L.; Díaz, D.; Zumeta-Dubé, I.; Arriola-Santamaría, H.; Betancourt, I.; Santiago-Jacinto, P.; Nava-Etzana, N. *Inorg. Chem*. **2013**, *52*, 10306-10317.

[19] Song, J.-H.; Nam, J.-H.; Cho, J.-H.; Kim, B.-I.; Chun, M.-P. *J. Korean Phys. Soc.* **2011**, *59*, 2308-2312.

[20] Moniz, S. J. A.; Quesada-Cabrera, R.; Blackman, C. S.; Tang, J.; Southern, P.; Weaver, P. M.; Carmalt, C. J. *J. Mater. Chem. A* **2014**, *2*, 2922–2927.

[21] a) Schiwon, R.; Metzinger, R.; Pfirrmann, C.; Limberg, C. *Z. Naturforsch.* **2013**, *68b*, 561–568; b) Schiwon, R.; Schax, F.; Braun, B.; Limberg, C. *J. Organomet. Chem.* **2016**. DOI: 10.1016/j.jorganchem.2016.02.041

[22] Pisarevskii, A. P.; Martynenko, L. I.; Dzyubenko, N. G. *Zh. Neorg. Khim.* **1990**, *35*, 1489–1493.

[23] Park, T. J.; Papaefthymiou, G. C.; Viescas, A. J.; Moodenbaugh, A. R.; Wong, S.S. *Nano Lett.* **2007**, *7*, 766-772

[24] Shamir, N.; Gurewitz, E. *Acta Cryst.* **1978**, *A34*, 662-666.

[25] Singh, A.K.; Kaushik, S. D.; Kumar, B.; Mishra, P. K.; Venimadhav, A.; Siruguri, V.; Patnaik, S. *Appl. Phys. Lett.* **2008**, *92*, 123910.

[26] Landers, J.; Salamon, S.; Escobar Castillo, M.; Lupascu, D. C.; Wende, H. *Nano Lett.* **2014**, *14*, 6061−6065.

[27] Rusakov, V.; Pokatilov, V.; Sigov, A.; Matsnev, M.; Gubaidulina, T. *Mater. Sci. Eng. B* **2014**, *4*, 302-309.

[28] Sosnowska, I.; Peterlin-Neumaier, T.; Streichele, E. *J. Phys. C: Solid State Phys.* **1982**, *15*, 4835-4846.

[29] Escobar Castillo, M.; Shvartsman, V. V.; Gobeljic, D.; Gao, Y.; Landers, J.; Wende, H.; Lupascu, D. C. *Nanotechnology* **2013**, *24*, 355701.

[30] Kostiner, E.; Shoemaker, G. L. *J. Solid State Chem.* **1971**, *3*, 186-189.

[31] Park, T. J.; Papaefthymiou, G. C.; Moodenbaugh, A. R.; Mao, Y.; Wong, S.S. *J. Mater. Chem*. **2005**, *15*, 2099-2105.

[32] Ramirez, F. E. N.; Pasca, G. A. C.; Souza, J. A. *Physics Letters A* **2015**, *379*, 1549–1553.

[33] Giaquinta, D. M.; Papaefthymiou, G. C.; zur Loye, H.-C. *J. Solid State Chem.* **1995**, 114, 199-205

[34] Sheldrick, G. M. SADABS, University of Göttingen, Germany, **1996**.

[35] Sheldrick, G. M. SHELXS-97, University of Göttingen, Germany, **2013**.

[36] a) Sheldrick, G. M. SHELXL-2013, University of Göttingen, Germany, **2013**; b) Sheldrick, G. M. *Acta Crystallogr. C Struct Chem.* **2015**, *71*, 3-8.

[37] https://www.uni-due.de/~hm236ap/hoersten/home.html

Table of Contents Graphic and Synopsis

$[Cp(CO)_2Fe\text{-}Bi(OAc)_2]$ **1** is a promising *single source precursor* for nearly phase-pure bismuth ferrite particles while thermolysis of the slightly modified precursor $[Cp(CO)_2Fe\text{-}Bi(O_2C^tBu)_2]$ **2** yielded mixtures of different bismuth oxide phases, revealing the distinctive influence of molecular design in material synthesis. The resulting materials were characterized by XRD, TEM and EDX as well as FTIR- and UV-Vis spectroscopy. In addition, the magnetic behavior was probed by VSM and ^{57}Fe Mössbauer spectroscopy.

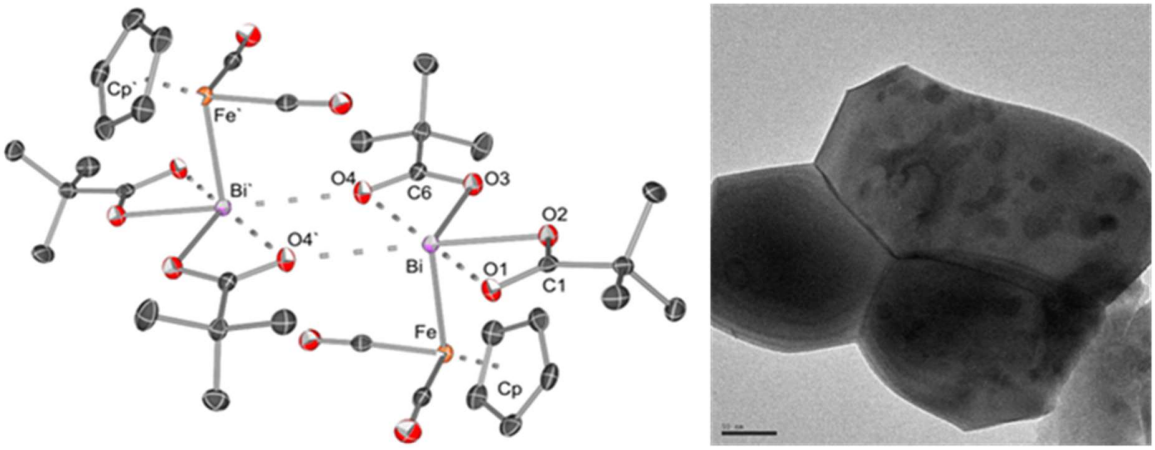

DOI: 10.1021/acs.inorgchem.6b00951
URN: urn:nbn:de:hbz:464-20201204-120541-0